G. A. Meehl · J. M. Arblaster · W. G. Strand Jr

Sea-ice effects on climate model sensitivity and low frequency variability

Abstract A change in a sea-ice parameter in a global coupled climate model results in a reduction in amplitude (of about 60%) and a shortening of the predominant period of decadal low frequency variability in the time series of globally averaged surface air temperature. These changes are global in extent and also are reflected in time series of area-averaged SSTs in the equatorial eastern Pacific Ocean, the principal components of the first EOFs of global surface air temperature and sea level pressure, Asian monsoon precipitations and other quantities. Coupled ocean-atmosphere-sea ice processes acting on a global scale are modified to produce these changes. Global climate sensitivity is reduced when ice albedo feedback is weakened due to the change in sea ice that makes it more difficult to melt. The changes in the amplitude and time scale of the low frequency variability in the model are traced to changes in the base state of the climate simulations as affected by modifications associated with the changes in sea ice. Making sea ice more difficult to melt results in increased sea-ice area, colder high latitudes, increased meridional surface temperature gradients, and, to a first order, stronger surface winds in most regions which strengthen near-surface currents, particularly in the Northern Hemisphere, and decreases the advection time scale in the upper ocean gyres. Additionally, in the North Atlantic there is enhanced meridional overturning due to increased density mainly in the Greenland Sea region. This also contributes to an intensified North Atlantic gyre. The changes in base state due to the sea ice change result in a more predominant decadal time scale of near 14 years and significantly reduced contributions from lower frequencies in the range of 15–40 year periods.

G. A. Meehl (✉) · J. M. Arblaster · W. G. Strand Jr
National Center for Atmospheric Research,
Boulder, Colorado 80307-3000, USA
E-mail: meehl@ncar.ucar.edu

1 Introduction

The possible role of the sea-ice parametrization in affecting global climate was demonstrated, for example, by Meehl and Washington (1990) when they showed that a change in the sea-ice albedo formulation resulted not only in different climate sensitivity to increased CO_2, but also in altered global atmospheric circulation. Bitz et al. (1996) and Yang and Neelin (1993, 1997) have demonstrated that altering sea-ice interactions with the ocean could affect decadal variability as well.

Meehl et al. (1998) suggest that the decadal time scale could be influenced by the mean circuit times in the ocean gyres, with those processes dependent on the base state of the climate system. They outlined the mechanism in the global coupled model analyzed here that contributes to global decadal variability of the climate system. The mechanism encompasses various regional decadal mechanisms outlined in previous studies (e.g., see review by Latif 1998, and references therein) involving advection of ocean heat content anomalies and coupled interaction between atmosphere and ocean in certain key regions to replenish those anomalies. The purpose of this work is to study how a change in a sea-ice parameter could affect that mechanism for low frequency variability and thus provide insight into how the climate system works.

Here, two simulations from the National Center for Atmospheric Research (NCAR) Department of Energy (DOE) global coupled GCM (Meehl and Washington 1995; Washington and Meehl 1996) are analyzed and compared to observations to identify links between the sea ice parametrization, globally averaged surface air temperatures, tropical Pacific SSTs, the thermohaline circulation in the ocean, and other aspects of the global climate system.

This work provides analyses of sensitivity studies to examine effects of changes in a sea-ice parameter on the global climate system. The sea-ice coupling to the atmosphere in this model using a sea-ice fraction threshold

is a very simple representation of such interactions, and subsequent model versions rely on more sophisticated techniques to perform this coupling. Thus this work is not meant as an advocacy study on the "best" sea-ice fraction threshold to use in coupled models. Rather, the change in sea-ice fraction threshold is a way to alter the way ice forms and consequently to cause changes to the climate base state which alter a decadal variability mechanism in the model. This study is a logical next step to follow up on earlier comparable experiments using more simplified non-dynamic slab ocean formulations with thermodynamic sea ice coupled to global atmospheric models (e.g., Meehl and Washington, 1990).

The integrations of the coupled model are relatively short in the context of low frequency variability. Both of the 76 year integrations examined below were meant to be control runs to be used as reference states to comparable length 1% per year compound CO_2 increase experiments. However, as stated, they are analyzed here as sensitivity experiments to examine the responses that occur in the climate system as represented by this particular global coupled model when a sea-ice parameter is changed. The resulting changes are dominant and systematic, giving us more confidence we are not just poorly sampling a chaotic system. We also provide a physical basis for expecting such changes in variability based on a mechanism for decadal variability in the model. Additionally, since the Coupled Model Intercomparison Project (CMIP) is set up to analyze integrations of this length as sensitivity experiments, the international climate modeling community has been able to extract useful information from such integrations. Future analyses with longer integrations of subsequent models will build on these initial sensitivity experiments to examine such effects in more detail.

2 The coupled model and experiments

The atmospheric component of the coupled model is an R15 L9 global spectral GCM, the ocean is a one degree by one degree 20L global ocean GCM, and the sea ice combines dynamic and thermodynamic schemes (Meehl and Washington 1995). This coupled model has been shown to accurately simulate most of the major surface current systems in the North Atlantic (Washington and Meehl 1996). Climate change in the tropical Pacific due to an increase of CO_2 also has been noted to resemble some aspects of ENSO in this model (Meehl and Washington 1996) with a slackening of the equatorial Pacific SST gradient and associated shifts of regional scale precipitation patterns that could have implications for fresh water resources in the Australasian region (Meehl 1996). These same patterns of climate change also have been shown to occur with a combination of increased CO_2 and sulfate aerosols in the coupled model (Meehl et al. 1996; Meehl et al. submitted 1999a). Low frequency variability in external forcing and the change in base state due to this forcing has been shown to affect low frequency global climate variability in this model as well (Meehl et al. 2000a).

In one of the coupled model simulations (labeled "M" here), the sea ice fraction threshold is set at 0.5. Half of the grid box must be ice free before the atmosphere "sees" an ocean albedo for that grid box. Thus it is relatively easy to melt ice (see discussions in Meehl and Washington 1990) since only half the grid box must be ice free

before the grid box albedo is set to the lower ice-free ocean value. This model configuration has a relatively high climate sensitivity to increased CO_2 (4.8 °C globally averaged surface air temperature increase in a transient CO_2 climate change experiment for a 10 year average at the time of CO_2 doubling around year 70). An experiment with the same atmospheric model coupled to a non-dynamic slab mixed layer produced an equilibrium warming due to a doubling of CO_2 of 4.6 °C (Washington and Meehl 1993). Thus the very large warming in this particular transient experiment (still far from equilibrium) already has a sensitivity that exceeds the equilibrium mixed layer. It has been shown that coupled interactions with the dynamical ocean, atmosphere and sea ice can significantly increase the sensitivity (Meehl et al. 2000b).

Earlier experience with mixed layer models (e.g., Meehl and Washington 1990) showed that climate sensitivity could be affected by altering parameters in the sea-ice formulation that changed the magnitude of ice albedo feedback. Thus in the second model integration (labeled "C"), the sea-ice fraction threshold is set at 0.75 (three-quarters of the grid box must be ice free before the atmosphere "sees" the lower ice-free ocean albedo for that grid box). This means in C it is, in general (and all other things being equal), easier to grow ice in the 0.25 to 0.5 range of ice coverage than it is in M mainly because incoming solar radiation is less effective in melting ice and ice albedo feedback is reduced as a consequence (e.g., Meehl and Washington 1990). As expected, in this integration there is a lower climate sensitivity to an increase of CO_2 (3.8 °C compared to 4.8 °C in the M integration). As will be documented later, there is thicker and more extensive sea ice as could be expected from the ice fraction formulation. However, there is an unanticipated affect on the decadal time scale variability in the coupled model that will be described.

The C experiment is allowed to stabilize for 59 years after the change in the sea-ice parameter from M, and the subsequent 76 years are then analyzed. At the end of the first 58 years after the sea-ice change, the globally averaged surface air temperatures had little trend, and there was little remaining secular change to most quantities in atmosphere and ocean.

3 Global coupled model simulations

As noted, the only change that was made between the two model integrations involved the ice fraction threshold, such that in the C experiment it was more difficult to melt sea ice, the ice albedo feedback was accordingly weakened, and the climate sensitivity was reduced. However, this change also has interesting consequences for the manifestations of decadal time scale variability between the two integrations.

Figure 1a, b shows the time series of globally averaged annual mean surface air temperature from the M and C experiments, respectively. Time series of smoothed (7 year running mean) annual mean globally averaged temperatures corresponding to the annual mean plots in Fig. 1a, b are shown in Fig. c and d, respectively. Area averaged Nino3 SSTs (from the eastern equatorial Pacific, 90W–150W, 5N–5S) are shown in Fig. 1e–f. Both M and C show greater-than-observed interannual and low frequency variability for globally averaged temperatures. The standard deviation is 0.45 °C for annual values for M in Fig. 1a, and 0.28 °C in Fig. 1b for C compared to standard deviation of detrended globally averaged annual mean surface temperatures for 1900–94 from the Jones (1994) data of 0.12 °C. For the 7 year running mean data, the standard deviation for M in Fig. 1c is 0.39 °C, and for C in Fig. 1c

▶

Fig. 1a–f Time series of global annual mean surface air temperature (from the lowest atmospheric model layer, sigma level 0.991, designated T991) for **a** the M experiment where sea ice is easier to melt, and **b** the C experiment where the sea ice is made more difficult to melt. Seven year running mean of global surface temperatures for **c** the M experiment, and **d** the C experiment. Seven year running mean of Nino3 SST for **e** the M experiment, and **f** the C experiment

a ANNUAL GLOBAL T$_{991}$, M

b ANNUAL GLOBAL T$_{991}$, C

c SMOOTHED GLOBAL T$_{991}$, M

d SMOOTHED GLOBAL T$_{991}$, C

e SMOOTHED NINO3 SST, M

f SMOOTHED NINO3 SST, C
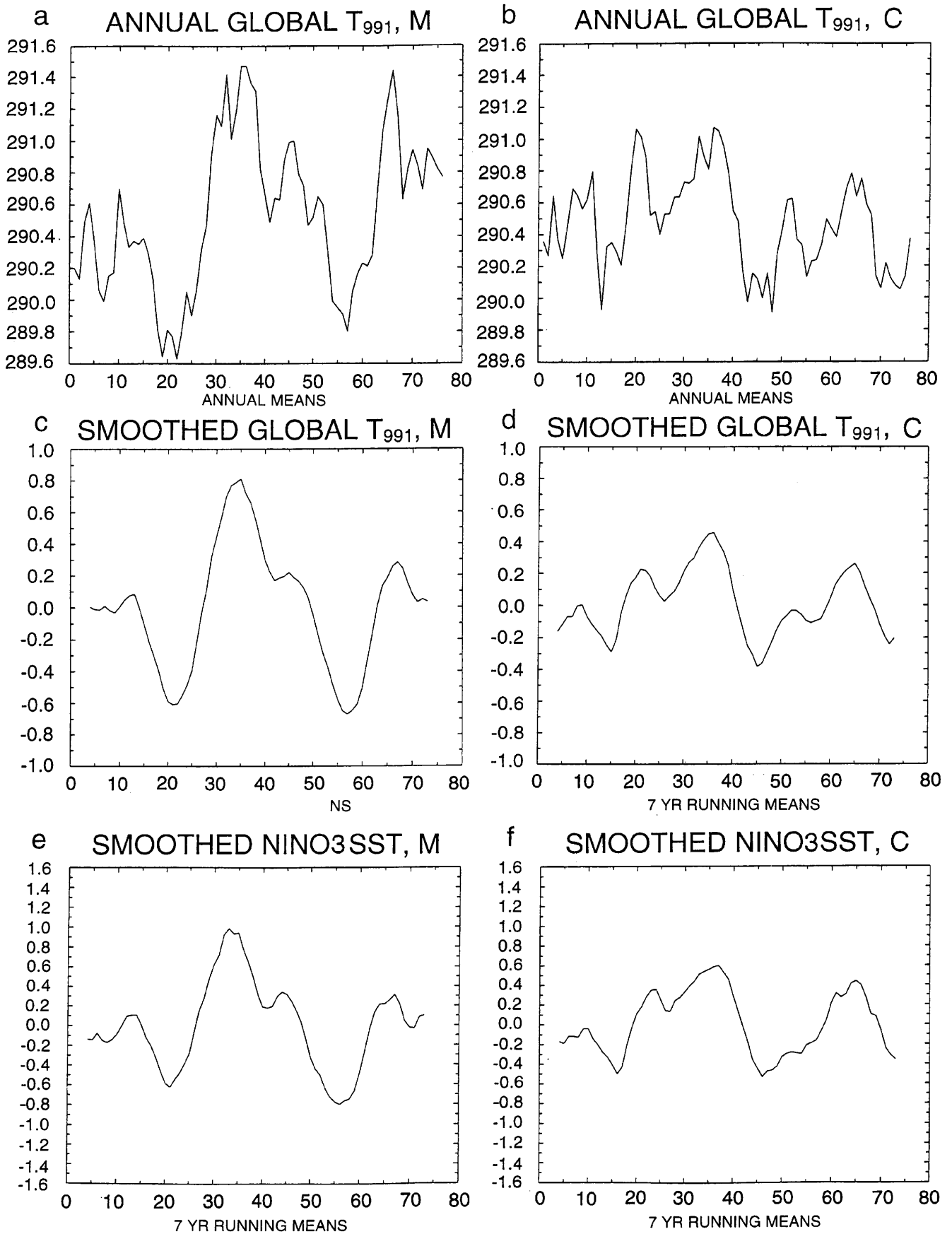
is 0.21 °C compared to the detrended 7 year running mean standard deviation for observed surface temperature data from 1900–94 of Jones (1994) of 0.07. Note the Jones (1994) data are near-global 2 m temperature over land and SST over ocean, while the global model data are from the first level above the surface. Comparison to model SST data shows similar patterns with small differences in magnitude.

However, the most striking difference between the two experiments is that the amplitude and time scale of the variability is different between the two. The amplitude of the decadal variability (for the 7 year running means in Fig. 1c, d) is about half the amplitude in C compared to M (standard deviation of 0.21 °C versus 0.39 °C as noted earlier). Additionally, the M experiment appears to have low frequency fluctuations that have an apparent period about twice as long as in the C experiment. The similarities of characteristics of the globally averaged time series in the two experiments are reflected in the Nino3 time series in Fig. 1. The Nino3 time series and globally averaged surface air temperature time series (Fig. 1a, b) are highly correlated with a correlation coefficient of +0.96 for the M experiment and +0.92 for the C experiment. Both are significant at greater than the 5% level taking into account autocorrelation in the time series and using 8 degrees of freedom from the 76 year time series following Leith (1973). A comparable calculation for the detrended observed globally averaged surface temperature time series (Jones 1994) from 1900–1994 has a correlation with Nino3 of +0.40 which is significant at greater than the 5% level again taking into account autocorrelation effects and using 36 degrees of freedom from the 95 year time series following Leith (1973). Note also that observed Nino3 amplitude and the implied relationship to global temperature undergoes low frequency variability as well (e.g. Webster et al. 1998). Though both model and observations display similar relationships, the model has higher amplitude decadal variability compared to the observed (Meehl et al. 2000a) which contributes to higher correlations.

To quantify the time scales of variability, Fig. 2 shows results from a spectral analysis of the globally averaged annual mean surface air temperatures for the M and C experiments. As suggested by the original time series in Fig. 1, the M low frequency (periods greater than about 15 years) spectra have greater power by about an order of magnitude, with considerable power at periods

ranging from about 15 to about 40 years. However, for the C experiment, the largest low frequency peak is around 14–15 years. Taking values for four frequencies representing periods from 15.2 to 38.5 years for M and C and performing an f test for eight degrees of freedom (Meehl et al. 2000a), the f value is 3.52 which is significant at greater than the 5% level, thus confirming the significantly enhanced low frequency variability in M compared to C.

To examine the patterns of variability, the first EOF of surface air temperature (calculated using the correlation matrix technique) is shown for the two experiments in Fig. 3 and for the observations (Jones 1994) in Fig. 4. Both model runs show general similarity to the observations (the "El Niño-like" pattern in the Pacific with large amplitude positive values in the central and eastern tropical Pacific, and opposite sign values in the far western, northwest and southwest Pacific). The first EOF from M explains more variance (34.9%) than the first EOF in the observations (13.6%), while the first EOF from C explains somewhat less than in M (25.4%). The time series of the principle components for the two experiments also show a strong connection to the time series of globally averaged surface air temperature as in the observations. For the M experiment, the correlation between the unsmoothed globally averaged surface air temperature and the unsmoothed time series of the first principle component is +0.70. For C the comparable correlation is +0.60. All are significant at greater than the 5% level taking into account autocorrelation effects and using 23 degrees of freedom following Leith (1973). The correlation for the unsmoothed time series for the observations is +0.81 which is significant at greater than the 5% level using 17 degrees of freedom following Leith (1973).

Plotted in Fig. 5 are the first EOFs of sea level pressure (SLP) from the two model experiments (explaining 22.5% of the variance

Fig. 2a, b Spectra of the time series of global annual mean surface air temperatures for **a** the M experiment shown in Fig. 1a, and **b** the C experiment shown in Fig. 1b. In *each panel* the *middle smooth line* is the red noise estimate, and *lower* and *upper smooth lines* are the 5% and 95% significance levels. Band width is the *length of line* in the *upper right hand* part of the panels. Note different scaling on *y axes*

a T$_{991}$ Global M

b T$_{991}$ Global C
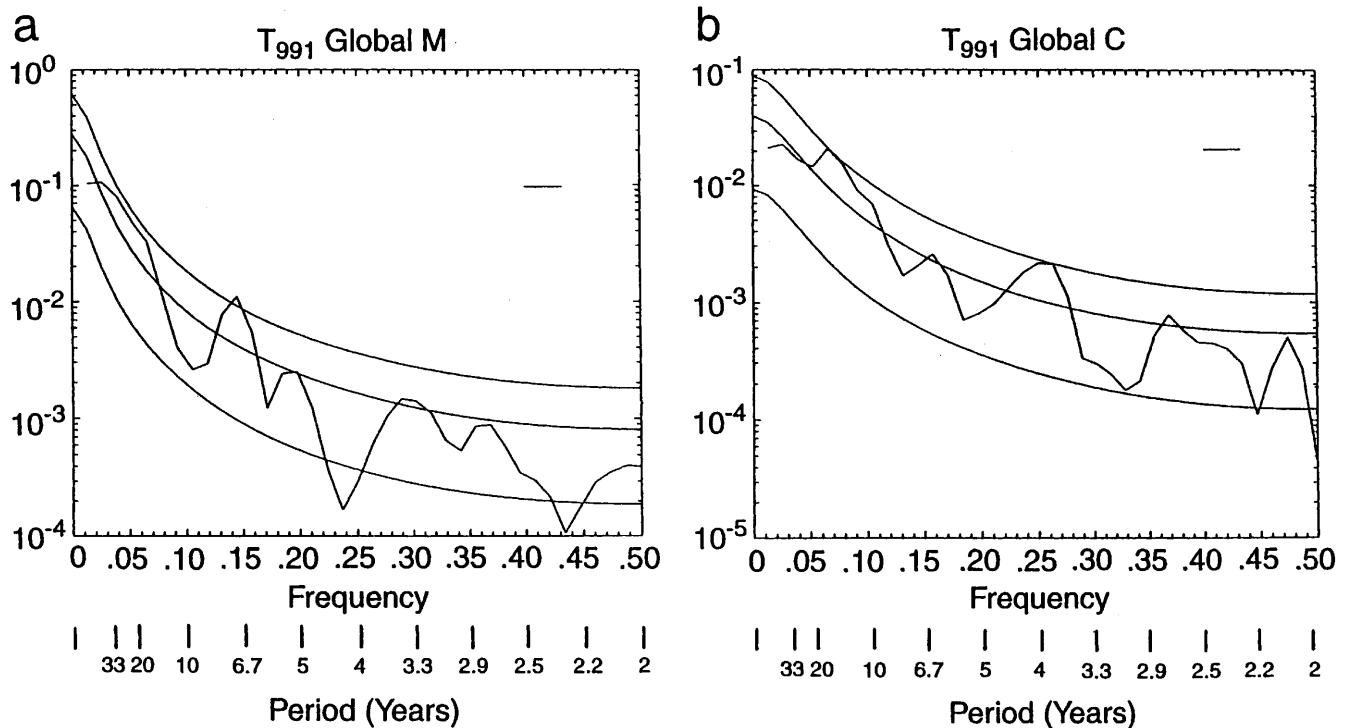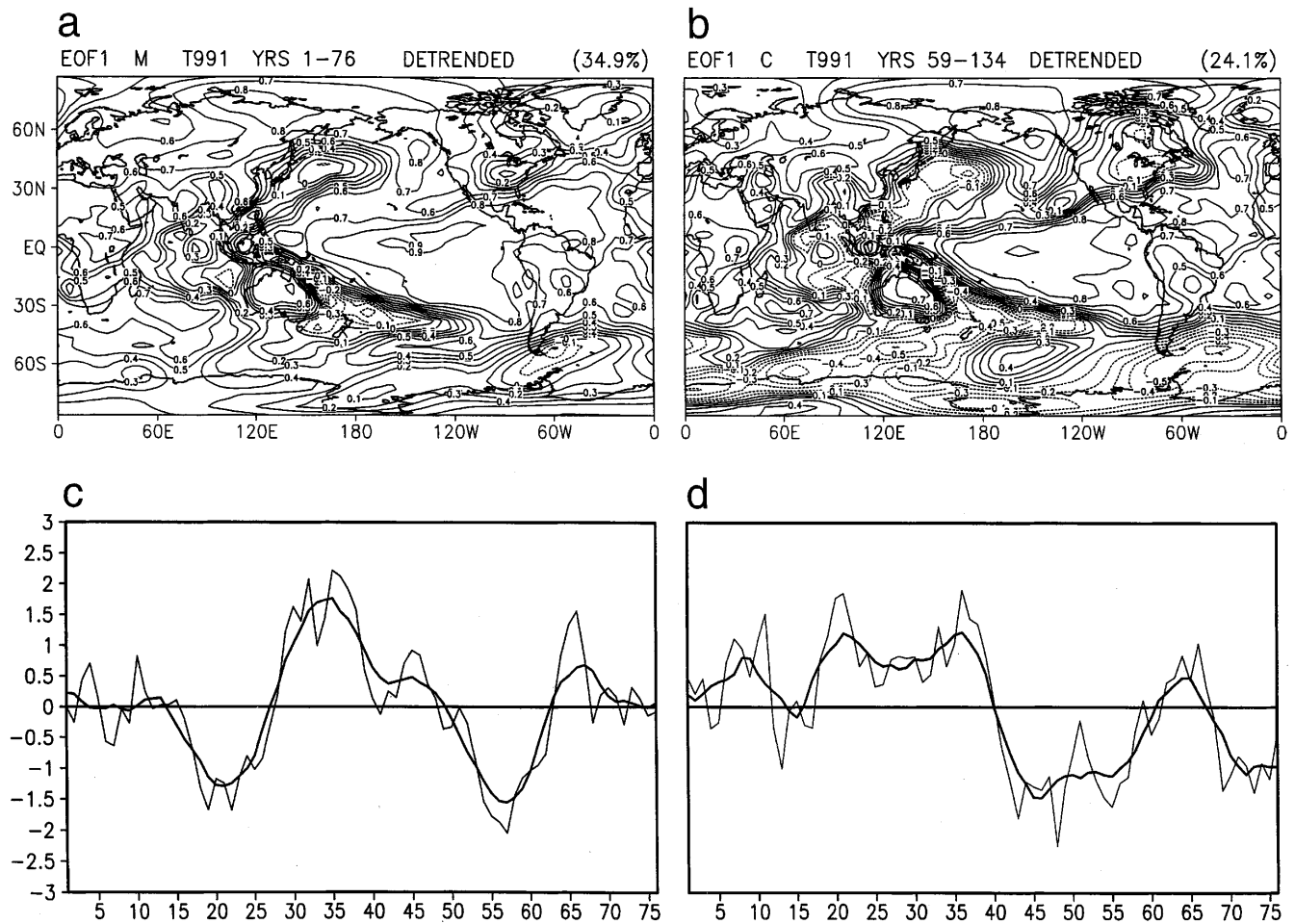
Fig. 3a–d The first EOF for surface air temperature from **a** the M experiment, **b** the C experiment, and the PC time series (annual values and seven year running means are shown) for **c** the M experiment shown in Fig. 3a, and **d** the C experiment shown in Fig. 3b

show results from filtered data with a cutoff at 8 years to separate the El Nino frequencies from the decadal in the model and observations. They confirm earlier observational results (e.g., Kang 1996; Zhang et al. 1997) that the El Nino-like pattern is present at both El Nino and decadal time scales.

for M, and 20.6% of the variance for C), and the time series of the first principle components. The observations are plotted in Fig. 6 (Kaplan et al. 2000). The first EOF of the latter explains 26.7% of the variance and agrees with both model experiments in that there is a dominant Southern Oscillation pattern, with large opposite sign values in the Pacific and Indian sectors in the tropics. The high frequency variability in the PC time series corresponds to ENSO with considerable low frequency variability as seen in the 7 year running mean in Fig. 6b. There are also links to the North Atlantic Oscillation with opposite sign anomalies between the subtropical and high latitudes in the North Atlantic region in both experiments. Correlation of the observed annual SLP EOF1 PC time series with the observed annual mean global temperature time series is +0.40 which is significant at greater than the 5% level using 53 degrees of freedom following Leith (1973).

Thus, when there is low pressure over the tropical Pacific, and high pressure over the Indian Ocean region with low pressure over the subtropical Atlantic and high pressure over the far north Atlantic, tropical Pacific SSTs and the globally averaged temperature both tend to be warm in the model and observations.

Both model simulations, like the observations, have a strong linkage between the amplitude of the pattern of global surface temperature and SLP variability with an "El Nino-like" signature in globally averaged surface temperature, which is stronger when comparing smoothed time series that emphasize the low frequency decadal time scale component of variability. Meehl et al. (1998)

4 Changes between the model integrations

Changing a sea-ice parameter results in changes in the base state that could affect the mechanism for decadal variability in the model. Figure 7 shows this change in base state for the long term mean (76 year) differences for C minus M. Though the relatively short integrations provide large signals of changes in base state, these states are, of course, characterized by decadal variability themselves. However, the changes in mean state are larger than the decadal variability signals. Mean increases in sea-ice area are associated with increases in albedo of around 0.03–0.06 or on the order of 5–10% at high latitudes in areas of sea-ice coverage in both hemispheres (Fig. 7a). In the high southern latitudes and most of the high northern latitudes (with the exception of the North Atlantic) this is accompanied by decreases of surface temperature of several degrees in Fig. 7b. Surface wind stress differences in Fig. 7c indicate enhanced westerlies near 50°S and 20°S in the Pacific of

a EOF1 Observed TS 1900−94 DETRENDED (13.6%)
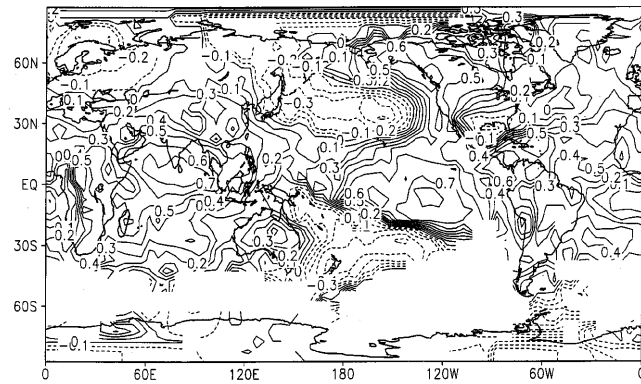
b
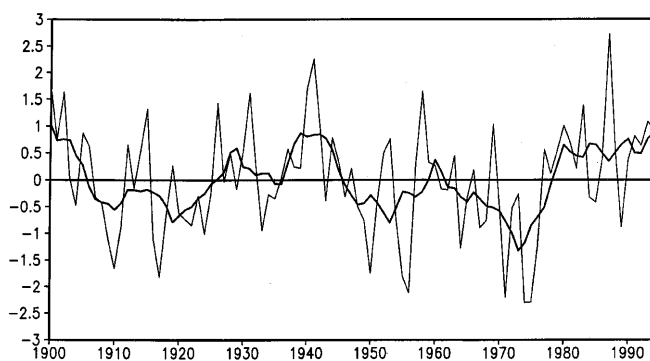
Fig. 4 a The first EOF of detrended observed surface temperatures (Jones 1994), 1900-94, and **b** the PC time series for the first EOF in Fig. 4a showing annual and seven year running mean values

about 0.01 N m^{-2} in association with the deepened circumpolar trough (on the order of 1 mb) and associated stronger SPCZ (not shown). However in the northern extratropics there are positive SLP differences of around 1.5 mb in the North Pacific in the Bering Sea resulting in a decrease of westerlies near 40°N (reduced westerly wind stresses of around 0.01 N m^{-2} or about 10%, Fig. 7c). There is stronger westerly surface wind stress near 50°N of about 0.02 N m^{-2} in the North Atlantic (Fig. 7c). The associated surface temperature differences in Fig. 7b in the North Pacific show positive differences near 50°N of about 1 °C in association with the weaker westerlies and consequent decreases of latent and sensible heat flux (not shown), and negative anomalies of about −0.3 °C near 25°N.

Precipitation differences in Fig. 7d reflect the circulation changes noted in Fig. 7c with a northeastward-shifted and intensified SPCZ in the southwest Pacific (positive differences of around 0.5 mm day^{-1}), reduced precipitation over Australasia, and increased precipitation over the North Atlantic in association with the deeper Icelandic low (not shown) and warmer surface temperatures (Fig. 7b).

In the North Pacific the enhancement of the meridional surface temperature gradient (colder high latitudes and warmer midlatitudes in Fig. 7b) could be

expected to produce increased baroclinicity there, enhanced extratropical cyclones, negative SLP anomalies, and stronger westerly wind stresses. Instead, there is a large area of positive SLP anomalies in the region of the Bering Sea (not shown) and easterly anomaly wind stresses (Fig. 7c). Part of the reason for this SLP response could be linked to the anomalous tropical precipitation patterns in Fig. 7d and their associated convective heating anomalies. Such anomalies have been shown to produce an anomalous Rossby wave response in the midlatitude North Pacific (e.g., Branstator 1983, 1990). For example, a perpetual January integration of an atmospheric model and fixed specified SSTs with a convective heating anomaly located at the equator on the dateline, in a location close to the largest positive precipitation changes in C in Fig. 7d (for further description of this experiment, see, e.g., Meehl et al. 1993) produces positive height anomalies over the Bering Sea and positive SLP anomalies in the North Pacific and weakened surface westerlies similar to those seen in Fig. 7c. Therefore there is some evidence of a combination of interacting tropical and midlatitude responses that produces the global temperature and circulation anomalies seen in Fig. 7 as a consequence of the sea-ice parameter change from M to C.

A significant difference between the M and C experiments noted briefly already in regards to the warmer and wetter conditions in C in the North Atlantic (Fig. 7b and d) has implications for the meridional overturning in the Atlantic that has been identified by, e.g., Mysak et al. (1990) as important for possible decadal time scale variability in that region. Figure 8 shows Arctic sea-ice thickness distributions illustrating the change in sea-ice mentioned such that there is roughly 25% more sea-ice coverage and about 45% thicker ice in C compared to M over the Arctic, including the North Atlantic, due to the parameter change that makes ice harder to melt in C.

In spite of this, the North Atlantic is warmer in C as opposed to the rest of the Arctic where colder conditions prevail compared to M (Fig. 7b). The fact that there is more sea ice but the North Atlantic is warmer seems counter-intuitive. But the reason can be traced to changes in the density structure of the North Atlantic. Figure 9 shows the density differences for C minus M. In association with more ice in the North Atlantic in C (Fig. 8), the entire region of the Greenland-Iceland-Norwegian (GIN) Sea is more dense in C compared to M (positive density differences) by about 0.5 to 1.0 kg m^{-3} (roughly 10–15%). This is due to the brine rejection process in forming sea ice during winter. As ice area increases in C, there is more brine rejection when ice freezes which acts as a salinity source to increase density and also intensify meridional overturning (e.g., note description of this mechanism in Yang and Neelin 1993, 1997). Yang and Neelin (1993) note that the period as well as the amplitude of this feedback process can be affected by various processes. Notably, in their simple model if the ice damping coefficient is increased, the
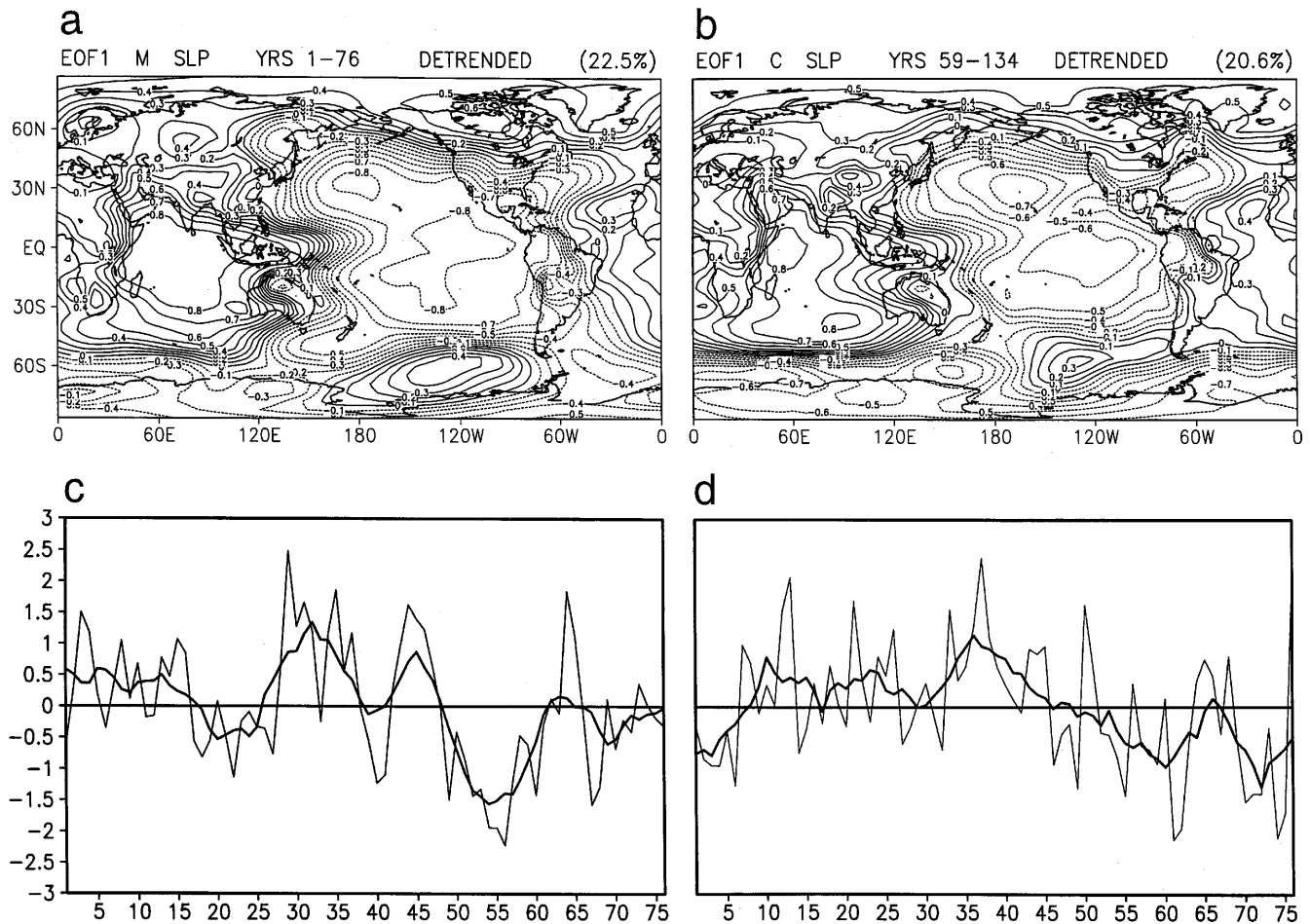
Fig. 5a–d Same as Fig. 3 except for SLP for the M and C experiments

amplitude of oscillation decreases. In the global coupled model considered here, sea-ice feedback acts to amplify the forcing signal (Meehl et al. 2000b), consistent with the larger amplitude oscillations for the more reactive sea ice formulation in M.

As shown in Fig. 10 (zonal mean meridional overturning for the Atlantic sector mid and high latitudes), there are negligible positive values of meridional overturning north of about 65°N in the GIN sea latitudes in M in Fig. 10a, while in C there is about +2 Sv sinking north of 65°N, with recirculation that overflows the sill at 65°N to join the sinking taking place near 60°N. Note that the values of Atlantic meridional overturning near 45°N are larger in C than M. An index of meridional overturning (zonal average from 30°N to 60°N, 300 m to 1500 m) shows a mean increase of overturning magnitude of 5.5 Sv or 31% in C compared to M. This strengthening of meridional overturning for the entire Atlantic is consistent with the results of Böning et al. (1996). They found, for a stand-alone Atlantic Ocean model with the northern boundary of the model near at 65°N, that not allowing any restoring at the northern boundary (to represent cutting off circulation contributions from the GIN Sea) reduced the strength of the

overall meridional overturning in the Atlantic by about 30% compared to a run where there was restoring at the northern boundary so as to include a representation of circulation contributions from the GIN Sea.

The strengthened meridional overturning in C contributes to increased heat and salt transport to the North Atlantic and thereby provides a positive feedback for maintaining warmer but more dense water at those latitudes. The additional salt transport, added to the brine rejection from the sea ice (in the model there is virtually no net annual ice transport from the Arctic into the GIN Sea, thus providing little fresh water flux from that source), contributes to increased density in C compared to M. However, the warmer water in the North Atlantic in C (Fig. 7b) is associated with increased evaporation and precipitation (Fig. 7d), and an 8% increase of precipitation minus evaporation averaged over that region which acts to decrease density. Yet, the contribution from brine rejection from the increased sea ice and the additional northward salt transport from the intensified meridional overturning ends up producing higher density in C and maintains the stronger meridional overturning (Delworth et al. 1993). This is shown in more detail in Section 5 below. In spite of the warmer SSTs in C in the North Atlantic, the water cools sufficiently in winter to freeze ice, and the change in sea-ice fraction

a EOF1 Observed SLP 1900–92 DETRENDED (26.7%)

b
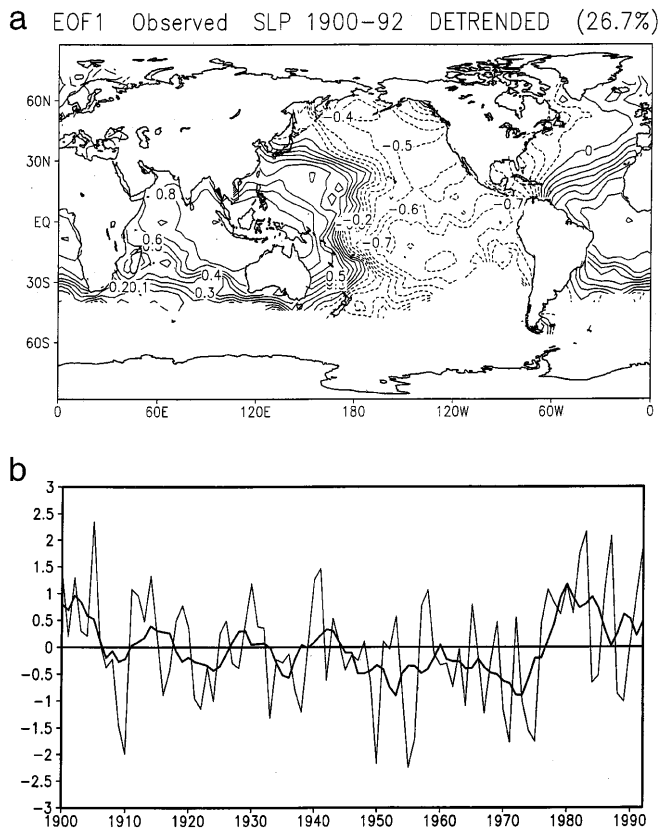
Fig. 6a, b Same as Fig. 5 except for observed SLP (Kaplan et al. 2000)

threshold allows ice to form more easily in C compared to M.

5 Change in base state and the global decadal oscillation

To determine why the nature of low frequency decadal timescale variability changed with the change in sea-ice parameter between M and C, the likely mechanism that produces the decadal time scale variability (Meehl et al. 1998) is revisited. Figures 11–13 depict lag correlations (lags of 13 years plus and minus) of various key parameters, associated with producing the decadal variability in the coupled model relevant to the present study, with globally averaged surface air temperature. All time series have first been low pass filtered with a 7 year running mean to emphasize the low frequency variability in the time series. These lag correlations expand upon the Meehl et al. (1998) study, and provide links to the changes in base state and decadal variability in the present experiments.

The solid lines in Fig. 11a, b are plots of the globally averaged surface air temperature time series from M and C, respectively, lagged with themselves. As could be expected from the spectra in Fig. 2, the period of the decadal oscillation is shorter by about 10 years in C than in M. In M in Fig. 11a, heat transport averaged across

45°N leads globally averaged surface temperature by about 6 years, though the correlations are less than 0.5 prior to the peak in temperature. The index of meridional overturning or thermohaline circulation (THC) in the Atlantic (labeled "Atlantic THC" in Fig. 11c) slightly leads heat transport in Fig. 11a and Labrador Sea density in Fig. 11c in the M experiment by a couple years, such that strong Atlantic THC and a maximum of density in the Labrador Sea is followed by strong northward heat transport and a peak in globally averaged surface temperature. Though it was shown in Fig. 10 that there is little ocean circulation contribution to northward ocean heat transport north of about 65°N in M compared to C, the weak heat transport at 65°N that does occur is roughly in phase with the globally averaged temperature in Fig. 11a.

In C in Fig. 11b, the more vigorous THC noted in Fig. 10b is associated with shorter period oscillations of heat transport at 45°N and 65°N compared to M in Fig. 11a, and both are more in phase with the globally averaged surface air temperature. There is a less strong association in C with the Atlantic THC index in Fig. 11d with maximum THC strength and Labrador Sea density leading heat transport and global temperature. However, the contribution of meridional overturning in the GIN Sea seen in Fig. 10b in C compared to little overturning there in M in Fig. 10a is manifest by a linkage between an index of meridional overturning in the GIN Sea ("GIN Sea THC" in Fig. 11d) with a maximum of density in the GIN Sea leading relatively larger values of GIN Sea overturning prior to and coincident with the maximum of globally averaged surface air temperature.

The stronger linkage in C in Fig. 11b and d between heat transport and GIN Sea density and overturning compared to M in Fig. 11a and c, and the shorter period in C of these quantities compared to M, points to the decadal mechanism outlined by Yang and Neelin (1993, 1997). They explored the chain of processes whereby as ice freezes and brine is released, density increases, the THC is strengthened, warmer water is transported northward, ice melts thus decreasing density, the THC weakens, and so on. They showed that if the THC is strengthened, the period of the decadal oscillation is shortened. Since the THC in C is stronger than in M with greater communication of circulation from the Atlantic to the GIN Sea, it is likely that such a chain of processes is occurring in the coupled model to contribute to reducing the amplitude and period of the decadal time scale oscillation in C compared to M.

These processes in the North Atlantic are associated with fluctuations of globally averaged quantities, not just with regional affects in the North Atlantic. Lag correlations of globally averaged surface temperatures with some parameters indicative of global radiative balance are plotted in Fig. 11e and f. Global absorbed solar radiation at the top of the atmosphere shows similar characteristics of a shorter period in C compared to M, and lead globally averaged surface air temperatures by about a year in both C and M. Lag correlations

Long Term Mean   C minus M
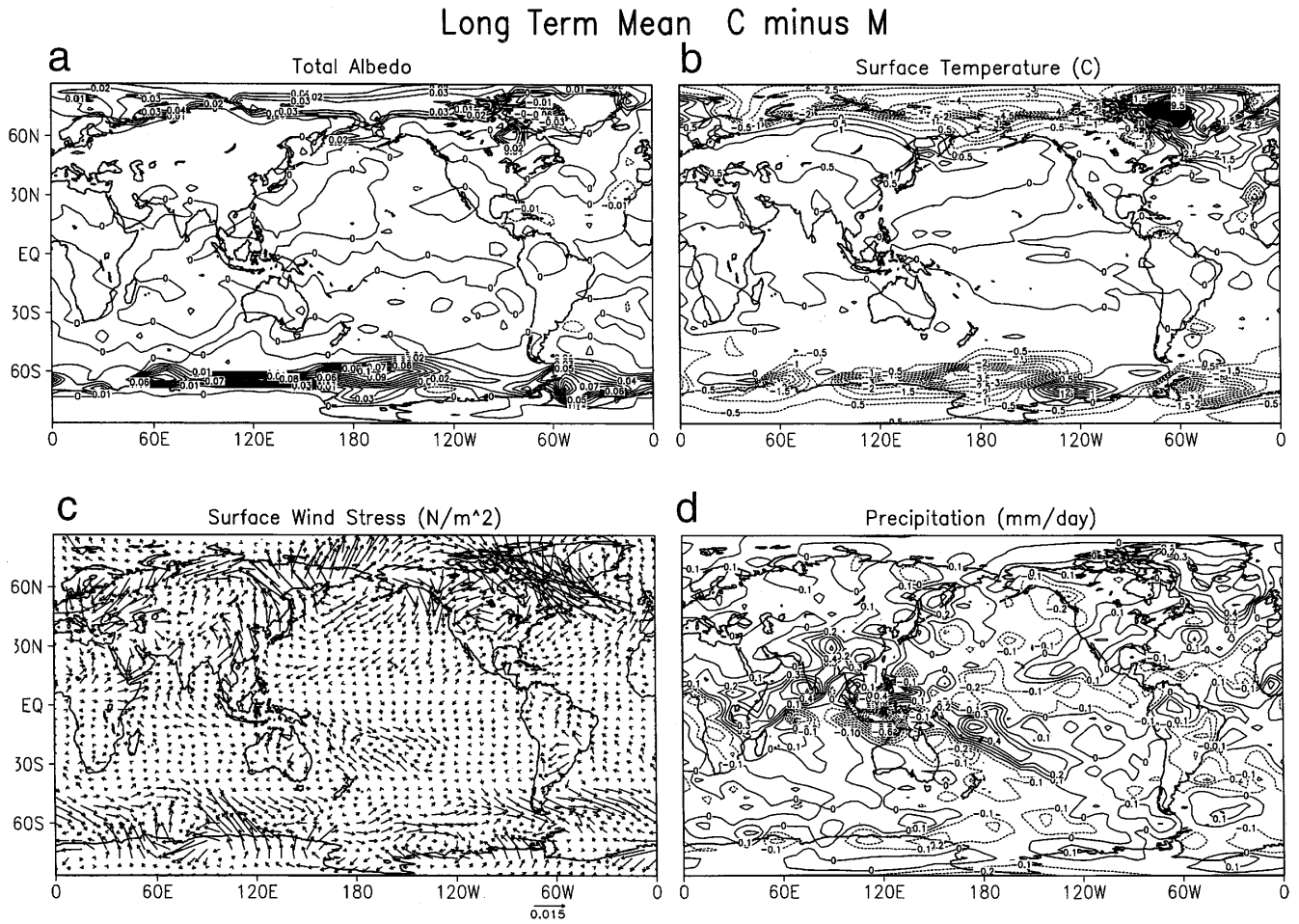
Fig. 7a–d Long term mean average from C (76 year average following the 59 year adjustment period after the sea-ice change) minus long term mean (76 year) average from the M experiment, for **a** planetary albedo, **b** surface air temperature, **c** surface wind stress, and **d** precipitation

with total sea-ice area are plotted for M and C in Fig. 11e and f, respectively. Again, the period for fluctuations in sea ice reflects that for globally averaged

surface air temperature with a minimum in total ice either coincident with (in C in Fig. 11f) or lagging slightly (in M in Fig. 11e) the maximum of globally averaged surface temperature. Thus as the planet warms, ice melts and global albedo (also plotted in Fig. 11e and f) decreases. As could be expected, the changes in sea ice contribute greatly to the albedo changes at high latitudes (not shown). However, there is a strong contribution to

Fig. 8a, b Sea-ice thickness distributions (cm) for **a** the M experiment, and **b** the C experiment

Sea Ice Thickness
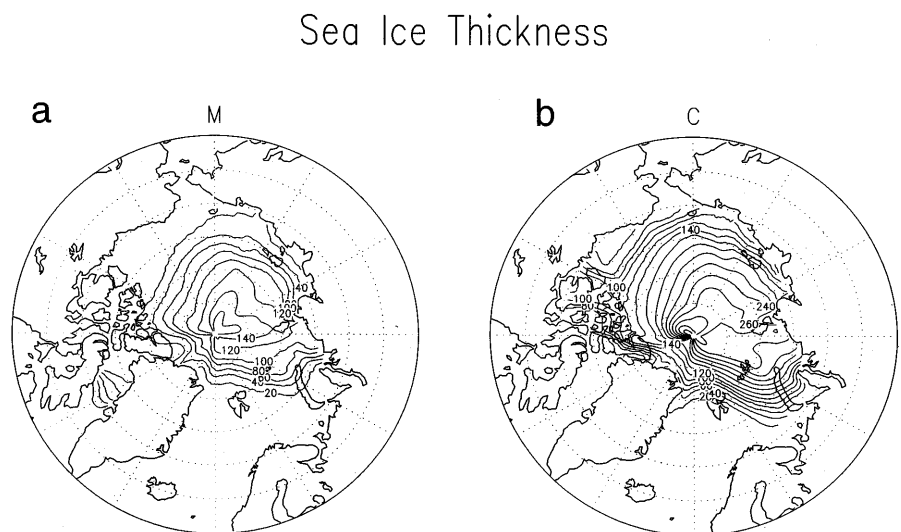
Fig. 9 Density difference (kg m^{-3}) for the C experiment minus the M experiment

the decrease in global albedo from the latitudes between 55°S and 55°N. At those latitudes changes in cloudiness, not ice changes, are affecting albedo. In fact, changes in albedo from 55°S to 55°N slightly lead globally averaged surface temperature by 2 years in M in Fig. 11e, and by about a year in C in Fig. 11f (low albedo in the latitudes averaged from 55°S to 55°N is associated with high values of global absorbed solar radiation and a maximum of globally averaged surface air temperature, see Meehl et al. 1998). Thus, the high latitudes and the corresponding changes in base state involving ocean heat transport, ice freeze and melt, density changes, and meridional overturning, all contribute to the global decadal variability in M and C with the time scales consistent with the greater low frequency variability in M compared to C.

Figure 12 shows lag correlations with globally averaged surface temperature of various quantities representing circulation and rainfall indices for tropical and midlatitude features that are associated with the decadal time scale fluctuations of globally averaged surface temperature (Meehl et al. 1998). As noted in Fig. 11, all quantities reflect the change in base state and resulting shorter period of oscillations in C compared to M. Additionally, the "El Niño-like" characteristics noted in Fig. 3 are also present. In both C and M, area-averaged precipitation in the central equatorial Pacific (5°N to 5°S, 150°E to 170°W) peaks about 1–2 years before the maximum of globally averaged surface temperature. Meanwhile, as in ENSO events, area averaged Asian monsoon precipitation (land points only averaged in the area 5°N to 40°N, 60°E to 100°E) is decreased at the same time, and the troughs in the northwest (area averaged SLP from 30°N to 50°N, 160°E to 180°E) and southwest (area averaged SLP from 30°S to 50°S, 180°
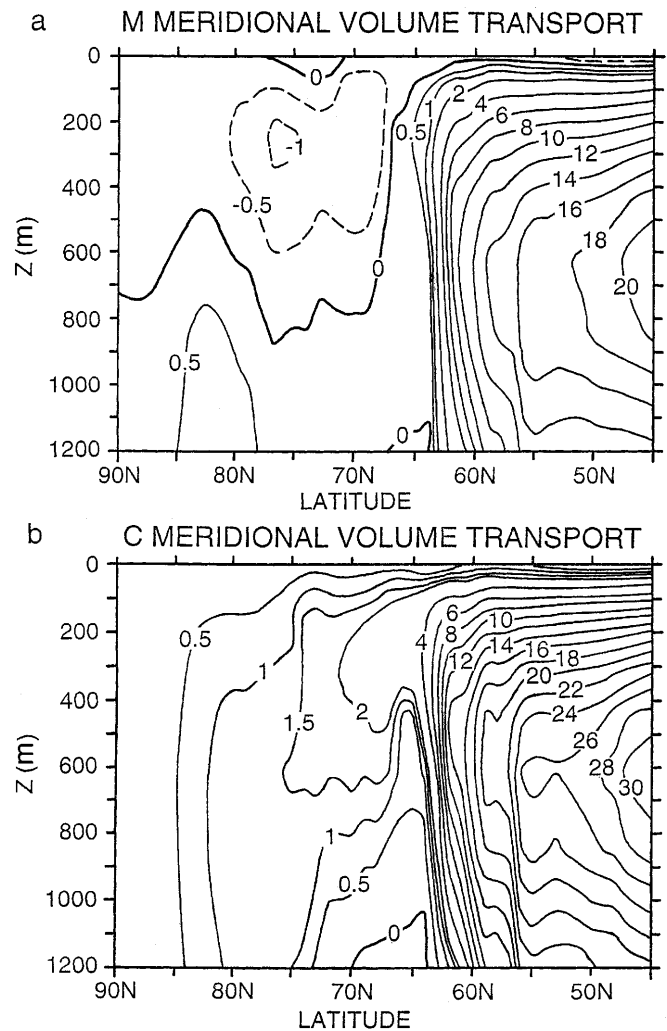
Fig. 10a, b Meridional overturning stream function (Sv) for the North Atlantic for **a** the M experiment, and **b** the C experiment

to 160°W) Pacific in Fig. 12a, b are negatively correlated (values of near −0.9 for M, and around −0.7 for C) with globally averaged surface temperature and lead by 1–2 years (as noted in Fig. 5). Meanwhile, in both M and C Nino3 SST and tropical (30°N to 30°S) 500 mb temperature both peak nearly coincident with the maximum of globally averaged temperature (Fig. 12c, d). Vertically averaged temperature (VAT) computed over the top 300 m of the ocean (a measure of ocean heat content) also reaches maximum correlations of about +0.8 for M in Fig. 12c, and near +0.7 for C in Fig. 12d, nearly coincident with the maximum of Nino3 SST and globally averaged surface temperature.

The response of the tropical Pacific SSTs in this model under various conditions that produce warming

▶

Fig. 11a–f Lag correlation plots for various index quantities labeled on the figure lagged with globally averaged surface air temperature for the M experiment (*left column*, **a**, **c** and **e**), and for the C experiment (*right column*, **b**, **d** and **f**). Data were first low pass filtered with a 7 year running mean
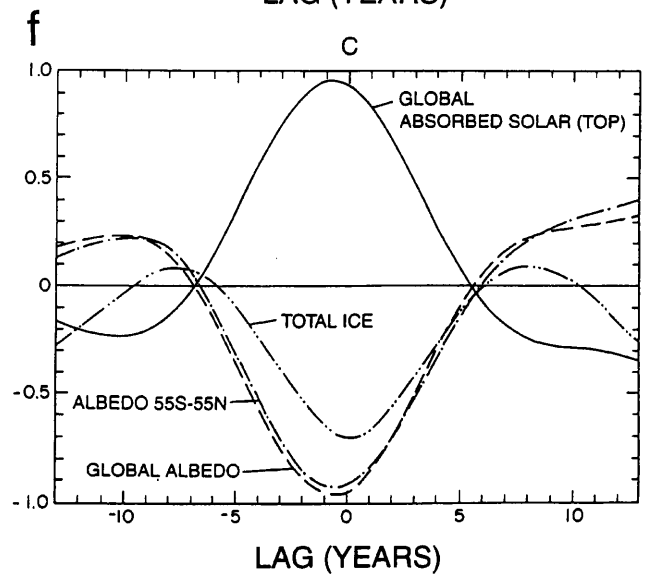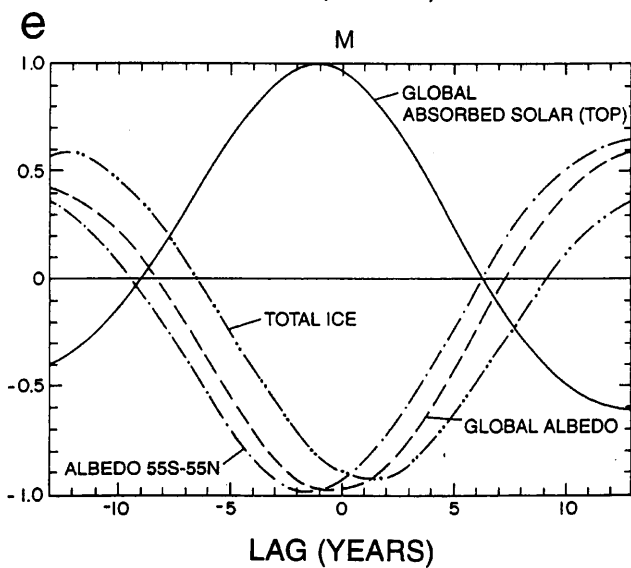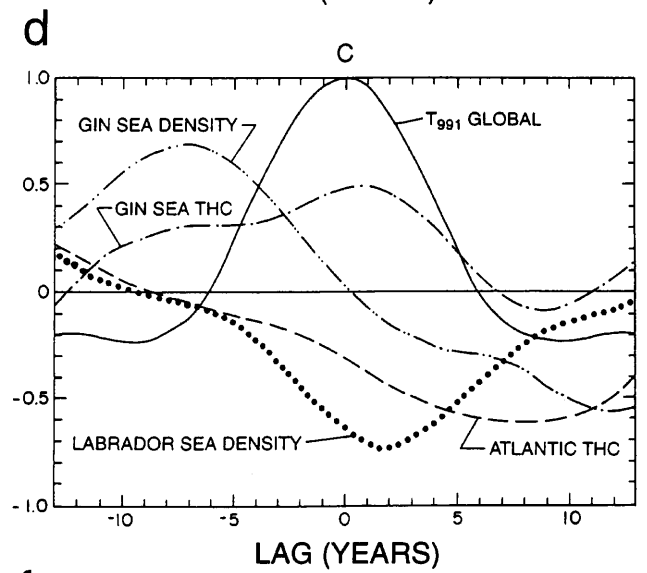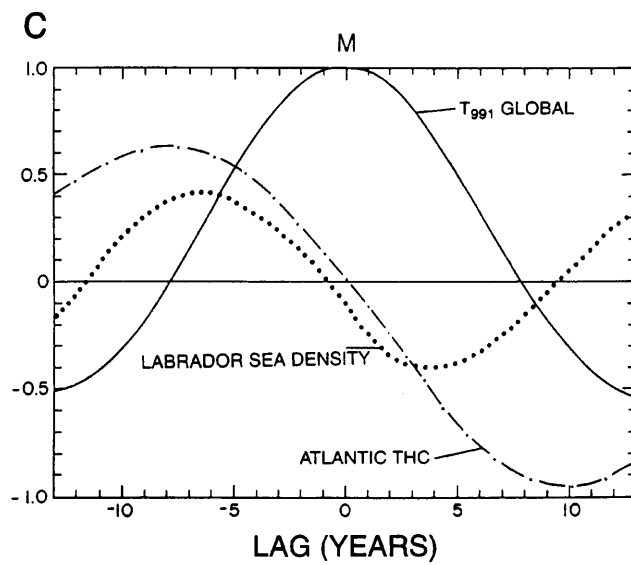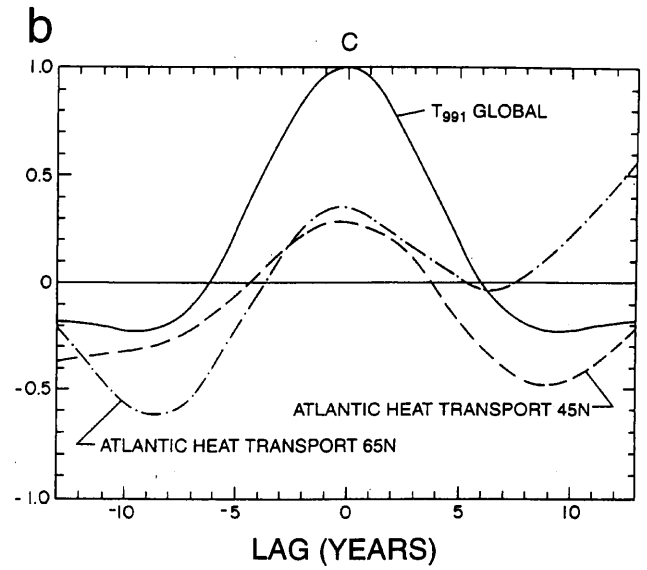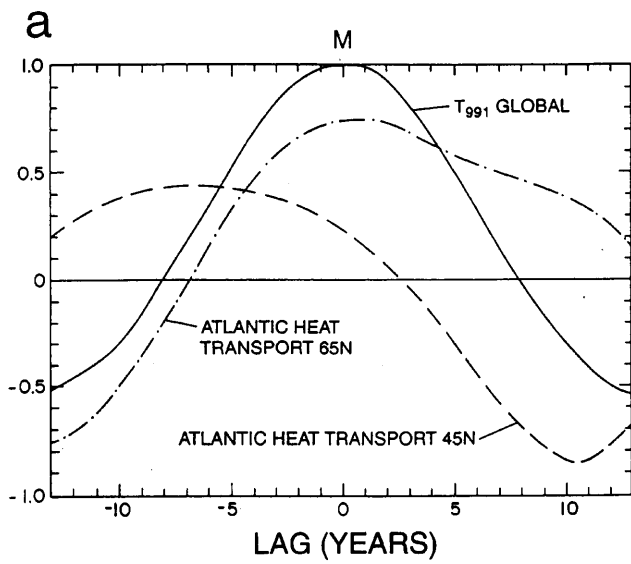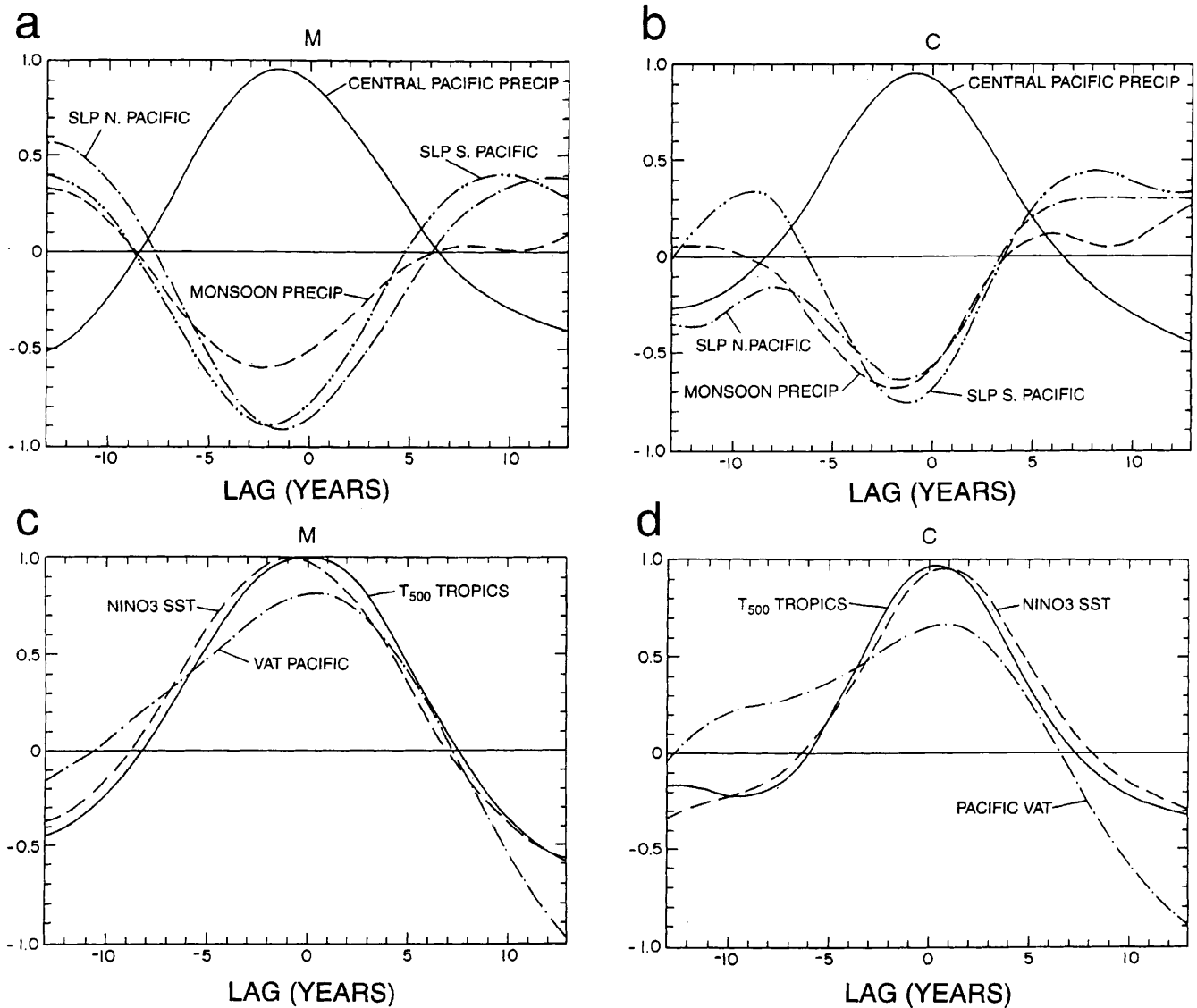
Fig. 12a–d Same as Fig. 11 for experiment M lag correlations with globally averaged surface air temperature in the *left column* (**a** and **c**), and the C experiment lag correlations in the *right column* (**b** and **d**)

have been documented by Meehl and Washington (1995, 1996) and Meehl et al. (2000b). Basically there is an asymmetry in the cloud radiative forcing that contributes to the eastern Pacific warming proportionately more than the western Pacific. These conditions are noted for the decadal time scale oscillation in Fig. 13 where area averages from the western equatorial Pacific (5°N–5°S, 140°E–170°E) and eastern equatorial Pacific (5°N–5°S, 120°W–90°W) of various quantities are lag correlated with globally averaged temperature. SST in the western and eastern Pacific warm along with globally averaged temperatures, but as suggested by the pattern of EOF1 in Fig. 3 the eastern Pacific warms more than the west. As noted by Meehl and Washington (1995, 1996) as SSTs increase there is a net negative change in cloud radiative forcing in the west and a positive change

in the east. This is associated with a positive correlation with planetary albedo in that region during times of increasing SST in both M and C (Fig. 13a, b). This combination of cloud feedbacks contributes to changes in radiation budget and an El Niño-like response on the decadal time scale with more warming in the eastern Pacific than the west during the warm phase.

However, ocean heat transport at 30°N across the longitudes 130°E to 180°E in Fig. 13a, b, roughly representing heat transported northward in the western Pacific by the Kuroshio current, decreases as global temperatures (and tropical Pacific temperatures) warm, with correlations of around −0.4 to −0.5 slightly leading the maximum in temperature in M, and slightly lagging in C. Heat transport by that current system in the Pacific is quite different from, and almost out of phase with, northward ocean heat transport in the Atlantic in Fig. 13. This point will be revisited in the discussion.

Meehl et al. (1998) noted that the time scale of the decadal oscillation is influenced in part by the mean
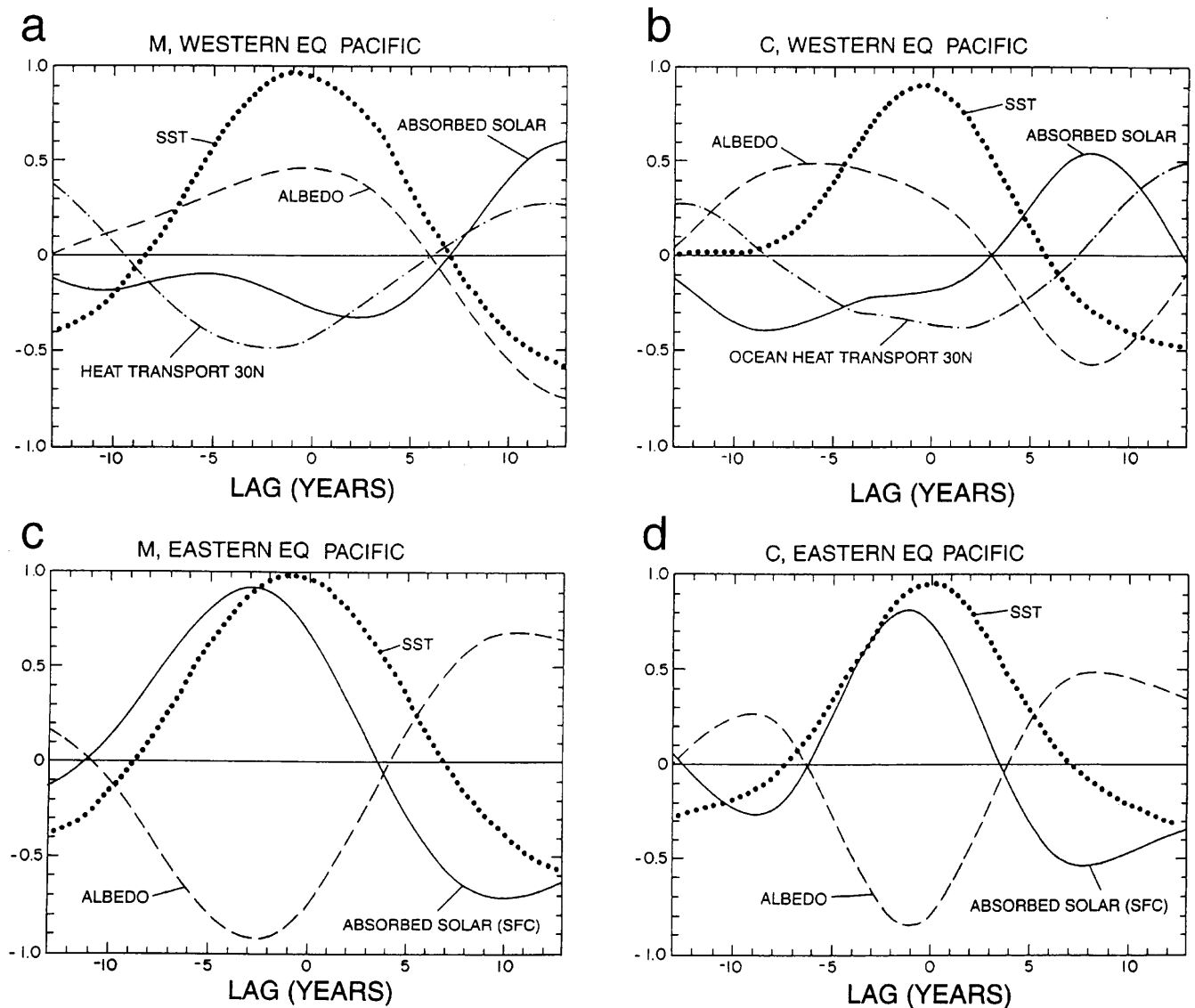
Fig. 13a–d Same as Fig. 11 except for quantities in the equatorial Pacific

circuit times in the various gyres. Figure 14 shows zonally averaged u-component surface currents in various latitude bands representing the major ocean gyre circulations (Meehl et al. 1998). Values are plotted for M, and for the incremental change in C. For the Northern Hemisphere ocean circulation systems, the flow in C is seen to be enhanced from that in M (by around 15% for zonal currents north of 20°N, and by 84% for the tropical return flow from 7°N–20°N). Near equatorial currents from 0° to 7°N are not plotted due to their strong vertical shear. In the tropics south of the equator the zonal surface currents are strengthened by over 2%, and farther south there is little change. Thus, the greatest contributions to enhanced zonal mean ocean gyre circulations are in the Northern Hemisphere. Results for vertically integrated currents in the upper 75 m show similar results, with somewhat greater increases in

the northern gyres (greater than 20%). This is similar to the result obtained in this model in a future climate change experiment where effects of increased CO_2 and sulfate aerosols are included (Meehl et al. 2000a). In that experiment, a weakening of the the Northern Hemisphere and tropical ocean circulations also reduce the amplitude of 10–20 year decadal surface temperature variability.

6 Conclusions

Two integrations of a global coupled GCM are analyzed, the only change between the two model simulations being a sea-ice parameter that is altered. One effect of this change, anticipated in the context of earlier model experiments with atmospheric models coupled to mixed layer oceans, is to reduce the contribution of ice albedo feedback to climate sensitivity. Consequently, climate sensitivity is reduced from 4.8 °C to 3.8 °C in transient
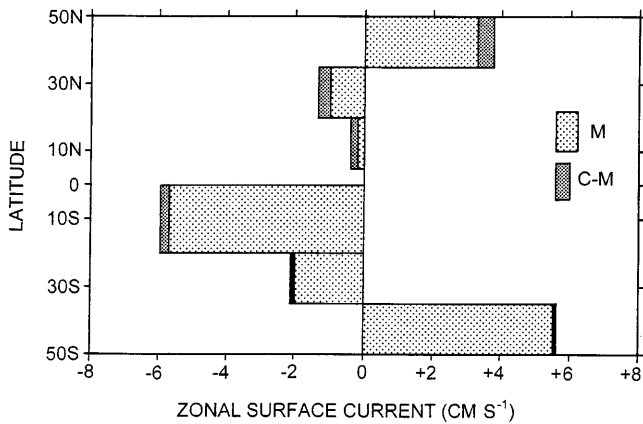
Fig. 14 Zonally averaged surface currents for latitude bands noted in the figure. *Light stippled values* are for the M experiment, *dark stippled areas* designate the experiment C minus experiment M values where the zonal currents in C are stronger than in M. *Blackened areas* for Southern Hemisphere currents indicate little change between M and C

CO_2 increase experiments at the time of CO_2 doubling around year 70.

Another more interesting effect is that the amplitude of low frequency (roughly 15–40 year period) variability is changed. It is shown that this different low frequency variability receives contributions from two factors, both involving changes in the climate base state. The first is the opening of ocean circulation via communication between the North Atlantic and the GIN Sea in the second experiment. This has the consequence of strengthening the meridional overturning in the Atlantic Ocean by about 30%, with an associated contribution to shortening the period and reducing the amplitude of decadal time scale variability documented in earlier model studies. The second involves a wider range of changes in base state related to increased sea ice area, decreased high latitude temperature, strengthened meridional temperature gradient, and increased magnitude of surface westerlies at most locations in the midlatitudes, associated with an eastward shift of precipitation in the tropical Pacific. These combine to contribute to increased mean strength of the ocean gyre circulations mainly in the Northern Hemisphere (along with the strengthened meridional overturning in the Atlantic which also plays a role in the enhanced gyre circulation in the North Atlantic). Thus, the advection of upper ocean heat content anomalies by the gyre circulations is enhanced, and the global coupled decadal mechanism contributes to the reduced amplitude and the emergence of the 14 year period as being the dominant time scale of low frequency variability in that experiment.

Though the duration of these integrations is relatively short, the changes are large, and they are related to a physical mechanism for decadal variability that is directly influenced by changes in the base state. Such effects need to be examined in more detail in subsequent longer integrations. Yet, the results presented here con-

firm earlier results with simpler models that a sea-ice parameter change (which produces changes in sea-ice extent larger than those associated with decadal variability over the past century) can have profound effects on the simulation of global climate. Additionally, these experiments raise the question of whether the effects of changes to external forcing (such as increased CO_2) could change the base state and consequent decadal variability in the climate system. Indeed, as mentioned already, analyses of a climate change experiment with this model show that the changes in base state from increased CO_2 result in a decrease in the amplitude of 10–20 year time scale surface temperature variability and increased amplitude of low frequency variability at periods longer than 20 years (Meehl et al. 2000a). Changes in the base state in the increased CO_2 experiment were comparable to those in the M experiment here, and suggest that mechanisms of climate variability can be affected by external forcing that significantly alters the climate base state.

References

Bitz CM, Battisti DS, Moritz RE, Beesley JA (1996) Low-frequency variability in the Arctic atmosphere, sea ice, and upper-ocean climate system. J Clim 9: 394–408

Böning CW, Bryan FO, Holland WR, Döscher R (1996) Deep water formation and meridional overturning in a high-resolution model of the North Atlantic. J Phys Oceanogr 26: 1142–1164

Branstator GW (1983) Horizontal energy propagation in a barotropic atmosphere with meridional and zonal structure. J Atmos Sci 40: 1689–1708

Branstator GW (1990) Mechanisms affecting the midlatitude atmospheric response to equatorial heating anomalies. International TOGA Sci Conf Proc, Honolulu, HI, 16–20 July 1990, WMO Geneva: 211–216

Delworth T, Manabe S, Stouffer RJ (1993) Interdecadal variations of the thermohaline circulation in a coupled ocean-atmosphere model. J Clim 6: 1993–2011

Jones PD (1994) Hemispheric surface air temperature variations: a reanalysis and an update to 1993. J Clim 7: 1794–1802

Kang I-S (1996) Association of interannual and interdecadal variations of global-mean temperature with tropical Pacific SST appearing in a model and observations. J Clim 9: 455–464

Kaplan A, Kushnir Y, Cane MA (2000) Reduced space optimal interpolation of historical marine sea level pressure. J Clim in press

Knutson T, Manabe S (1998) Model assessment of decadal variability and trends in the tropical Pacific Ocean. J Clim 11: 2273–2296

Latif M (1998) Dynamics of interdecadal variability in coupled ocean-atmosphere models. J Clim 11: 602–624

Leith CE (1973) The standard error of time-average estimates of climatic means. J App Meteorol 12: 1066–1069

Meehl GA (1996) Vulnerability of fresh water resources to climate change in the tropical Pacific region. J Water, Air Soil Pollut 92: 203–213

Meehl GA, Washington WM (1990) CO_2 climate sensitivity and snow-sea-ice albedo parametrization in an atmospheric GCM coupled to a mixed-layer ocean model. Clim Change 16: 283–306

Meehl GA, Washington WM (1995) Cloud albedo feedback and the super greenhouse effect in a global coupled GCM. Clim Dyn 11: 399–411

Meehl GA, Washington WM (1996) El Niño-like climate change in a model with increased atmospheric CO_2 concentrations. Nature 382: 56–60

Meehl GA, Branstator GW, Washington WM (1993) Tropical Pacific interannual variability and CO_2 climate change. J Clim 6: 42–63

Meehl GA, Washington WM, Erickson III DJ, Briegleb BP, Jaumann PJ (1996) Climate change from increased CO_2 and the direct and indirect effects of sulfate aerosols. Geophys Res Lett 23: 3755–3758

Meehl GA, Arblaster JM, Strand WG Jr (1998) Global scale decadal climate variability. Geophys Res Lett 25: 3983–3986

Meehl GA, Washington WM, Arblaster JM, Bettge TW, Strand WG Jr (2000a) Anthropogenic forcing and climate system response in sensitivity experiments of 20th and 21st century climate. J Clim in press

Meehl GA, Collins W, Boville B, Kiehl JT, Wigley TML, Arblaster JM (2000b) Response of the NCAR Climate System Model to increased CO_2 and the role of physical processes. J Clim in press

Mysak LA, Manak DK, Mardsen RF (1990) Sea-ice anomalies in the Greenland and Labrador Seas 1900-84 and their relation to an interdecadal Arctic climate cycle. Clim Dyn 5: 111–133

Washington WM, Meehl GA (1993) Greenhouse sensitivity experiments with penetrative cumulus convection and tropical cirrus albedo effects. Clim Dyn 8: 211–223

Washington WM, Meehl GA (1996) High latitude climate change in a global coupled ocean-atmosphere-sea ice model with increased atmospheric CO_2. J Geophys Res 101: 12 795–12 801

Webster PJ, Magana VO, Palmer TN, Shukla J, Tomas RA, Yanai M, Yasunari T (1998) Monsoons: processes, predictability, and the prospects for prediction. J Geophys Res 103: 14 451–14 510

Yang J-Y, Neelin JD (1993) Sea-ice interactions with the thermohaline circulation. Geophys Res Lett 20: 217–220

Yang J, Neelin JD (1997) Decadal variability in coupled sea-ice–thermohaline systems. J Clim 10: 3059–3076

Zhang Y, Wallace JM, Battisti DS (1997) ENSO-like decade-to-century scale variability: 1900–93. J Clim 10: 1004–1020